Xu *et al.*
Chinese Journal of Mechanical Engineering (2023) 36:90
https://doi.org/10.1186/s10033-023-00905-6

Chinese Journal of Mechanical Engineering

ORIGINAL ARTICLE

Open Access

NuBot: A Magnetic Adhesion Robot with Passive Suspension to Inspect the Steel Lining

Hao Xu[1], Youcheng Han[1], Mingda He[1], Yinghui Li[1] and Weizhong Guo[1*]

Abstract

The steel lining of huge facilities is a significant structure, which experiences extreme environments and needs to be inspected periodically after manufacture. However, due to the complexity (crisscross welds, curved surface, etc.) of their inside environments, high demands for stable adhesion and curvature adaptability are put forward. This paper presents a novel wheeled magnetic adhesion robot with passive suspension applied in nuclear power containment called NuBot, and mainly focuses on the following aspects: (1) proposing the wheeled locomotion suspension to adapt the robot to the uneven surface; (2) implementing the parameter optimization of NuBot. A comprehensive optimization model is established, and global optimal dimensions are properly chosen from performance atlases; (3) determining the normalization factor and actual dimensional parameters by constraints of the steel lining environment; (4) structure design of the overall robot and the magnetic wheels are completed. Experiments show that the robot can achieve precise locomotion on both strong and weak magnetic walls with various inclination angles, and can stably cross the 5 mm weld seam. Besides, its maximum payload capacity reaches 3.6 kg. Results show that the NuBot designed by the proposed systematic method has good comprehensive capabilities of surface-adaptability, adhesion stability, and payload. Besides, the robot can be applied in more ferromagnetic environments and the design method offers guidance for similar wheeled robots with passive suspension.

Keywords Wheeled robot, Passive suspension, Magnetic adhesion, Steel lining, Design method

1 Introduction

Currently, the nuclear power industry takes large adoption of steel lining construction as the inner wall of security containment, and that is the last barrier to prevent the radioactive substance from leaking in the nuclear accident [1]. Hence, it is very essential to inspect the sealing safety and welding reliability periodically, considering that the steel lining is a huge sealed container welded by thousands of weld seams for hundreds of curved steel plates. Traditional method for inspecting the steel lining weld is mainly relying on the worker's manual examination standing on the scaffold, bringing the demerits of long-period time, great difficulty, and high cost. Hence, it is significant and challenging to develop a robot platform for the (semi-)automatic inspection of steel lining welds. The relevant research priorities/problems are:

The wall-climbing and surface-adaptive locomotion mechanism to accommodate and move on the containment steel lining. The steel lining has a large curved surface with massive crisscross arc welds and obstructed surroundings, demanding that the robot should possess a capable locomotion mechanism and reasonable setup of degrees of freedom (DOF). In previous researches, the climbing robots include: a) the crawler robots need additional mechanisms to ensure the whole track fits the wall shape. Seo et al. [2] adopted active compliant joints

*Correspondence:
Weizhong Guo
wzguo@sjtu.edu.cn
[1] State Key Lab of Mechanical System and Vibration, School of Mechanical Engineering, Shanghai Jiao Tong University, Shanghai 200240, China

Table 1 Qualitative comparison of different types of climbing robots.

Adhesion	Example	Locomotion mechanism	Wall type	Adhesion force	Velocity	Payload	Terrain-adaptable	Wall-harmless	Build-in power
Magnetic	**NuBot (ours)**	Wheel	Steel	√	√	√	○	√	√
	Magnetic crawler [3]	Track		√	○	√	○	○	√
	HIT robot [11]	Leg		√	×	○	√	√	×
Pneumatic	MultiTrack [14]	Track	Smooth surface	√	√	√	○	○	×
	W-Climbot [4]	Leg		√	×	○	√	√	×
Mechanical	SpinyBot II [15]	Leg	Rough surface	×	×	×	×	×	√
	CSU robot [17]	Wheel		×	√	×	○	×	√
Electrostatic	SJTU robot [19]	Leg	Flat surface	√	○	√	○	○	×
Gecko-like		Wheel-leg	Smooth surface	○	○	○	√	√	√

to increase the preload on the front track; Gao et al. [3] adopted the linkage-spring system to connect two track modules. However, the active joint increases the number of actuators, and the hard metal track scratches the steel lining plating; b) the legged robots possess a larger workspace with better adaptability. Guan et al. [4] imitated an inchworm and proposed a biped serial climbing robot with five DOFs. Liu et al. [5] presented a robot with eight footpads and one active DOF, which could adapt to the wall curvature by a passive four-bar mechanism. However, the legged locomotion produces 19051270000dynamic adhesion-separation cycles between the footpad and terrain surface, resulting in a discrete gait slowing the speed; c) the wheeled robots with no more than three wheels [6–8] can always keep each wheel in contact with the wall. However, on one hand, more wheels are preferred to provide stronger adhesion force and larger driving force; on the other hand, more wheels can make many of them separate from the wall, unless the robot is designed with an adaptive suspension or compliant mechanism: Eto et al. [9] developed a passive rocker arm suspension and spherical wheels to adapt to the wall shape; Guo et al. [10] proposed a robot with an electromagnetically driven compliant beam to effectively negotiate corners. In conclusion, the wheeled robot with passive suspension is a feasible option, which offers sufficient DOFs to ensure that the wheels adapt to the wall without increasing actuators.

(1) *The stable and practical adhesive approach to attach to the containment steel lining.* Adhesion principles are the direct factor that determines the adhesion stability and payload. Table 1 compares five types of adhesive approaches in various aspects of performances, where √, ×, ○ indicate respectively that the robot can, basically can, cannot meet the current demands. Thereinto, magnetic adhesion [3, 6–8, 11–13] works well on a ferromagnetic surface, which is an effective choice for the steel lining. Generally, the adhesion force depends on the magnet material, size, shape, and distance from the wall. In contrast, pneumatic adhesion [4, 14] can be employed for more occasions. However, the required pump limits the minimum size and weight, and the adhesion force will decrease when the gap occurs between the adhesion mechanism and the curved wall. Mechanical adhesion [15–17] imitates the structure of insects in nature, such as claws, hooking tiny grooves on rough walls. Nevertheless, they cannot adapt to the steep and smooth wall of containment due to insufficient adhesion force. Electrostatic adhesion [18, 19] generates adhesion and actuation force by energizing the soft material. However, the current conducted to the wall increases the risk to cause nuclear accidents. Gecko-like adhesion [20, 21] relies on the van der Waals force between the footpads and the wall. However, this method is not workable because the dust on the surface of the containment affects the adhesion. Considering environmental constraints, the NuBot is expected to be endowed with good comprehensive capabilities of surface adaptability, adhesion stability, steel-lining surface harmlessness, locomotion velocity, lightweight with high integration of build-in power and other mechatronic devices. Based on the above analysis and demands, magnetic adhesion is the optimal option for the steel lining.

(2) *The systematic design method to develop the robot platform under the comprehensive operation demands.* In the environment of nuclear power containment, the adhesion robot is required with a big adaptive workspace for the varying terrains, good payload and stiffness, small size and weight. In

the climbing robot field, Zhang et al. [22] designed a passive adaptive moving mechanism utilizing the magnetic circuit optimization, and ensures the allowable motor torque in a stable operation mode; Liu et al. [23] optimized the footpad of a vertical-climbing robot for various curvatures according to the experiment-based Taguchi method; Song et al. [6] optimized the water-jetting wall-climbing robot with the optimum structure of magnetic adhesion system, etc. One can see there does not exist a systematic method for the overall optimization design of the climbing robot, considering the coupling relations among the size, workspace, adhesion force, driving force, stability, etc. Some works in the mechanism optimization field can provide a few references: Hoff et al. [24] optimized the bat-inspired biological robot for better flight characteristics after employing the principal component analysis; Liu et al. [25] proposed the performance-chart-based design methodology (PCbDM) as a general optimization approach to designing the less-parameter mechanism, obtained optimized parameters of a 3-DOF parallel manufacturing module [26], and investigated the 2T1R-type parallel mechanisms applying the Grassmann line geometry method [27]; thereafter, Li et al. [28] analyzed the influence of limb arrangements on the parasitic motion of 3-PRS parallel mechanism, and generated the singularity-free and high-performance workspace for a 3-DOF 2-CRRR-CRR parallel manipulator [29]; Han et al. [30] solved the sixteen-parameter optimization for the reconfigurable legged mobile lander, under the demands of multiple operation modes and multiple performance criteria, etc.

This paper proposes a magnetic adhesion robot called NuBot to inspect the steel lining weld on the nuclear power containment. As aforementioned, the magnetic adhesion wheeled robot with passive suspension is the optimal option under the special environment. Hence, this research will be mainly focused on the demand-oriented systematic design method for the NuBot from type identification to topology parameter optimization for the NuBot first, and then demonstrate the experimental validation based on the semi-automatic mechatronics system utilizing a proportional integral (PI) control strategy.

The rest of this work is organized as follows. Section 2 presents an overview of the robot platform and the design strategy. Section 3 describes the type design of the suspension, its kinematic model, and the overall robot dynamics. Section 4 presents the optimization design process. Overall parameters are obtained from non-dimensional to dimensional, from partial to global utilizing PCbDM. In Section 5, the unit design is completed and the prototype is developed. Locomotion and payload experiments are conducted in Section 6. Section 7 presents the comparison between several climbing robots. Finally, the conclusion is presented in Section 8.

2 Overview of the Robot Platform and Design Method

Figure 1(a) shows the nuclear power plant containment [1], which has a cylindrical ferromagnetic steel lining with a diameter of 37 m and a height of 61.6 m. Its surface is distributed with massive crisscross arc welds with a maximum height of 5 mm. The support structure inside the steel lining is only 0.2 m away from the wall, which limits the height of the robot. Besides, the adhesion force must be reliable because it is not allowable to attach the protective rope inside the containment. And the load of NuBot is required to be no less than 0.4 kg, including the controller, camera, communication equipment, battery, etc. Figures 1(b, c) show the structure of NuBot, including two passive suspensions, six magnetic adhesion wheels, the chassis, an image capture system, and a control system. When inspecting the weld seam inside the containment, the technician controls NuBot to move and monitor the images captured by the camera. During locomotion, the 3-DOF suspension ensures all wheels are in contact with the complex surface of steel lining, and adapt to the surrounding environment like support structure.

Figure 2 shows the structure of the magnetic adhesion wheel. Each wheel is driven independently with a built-in permanent magnet unit and a motor-reducer-encoder unit. It is connected to the suspension through a passive revolute joint, whose axis is perpendicular to the wheel

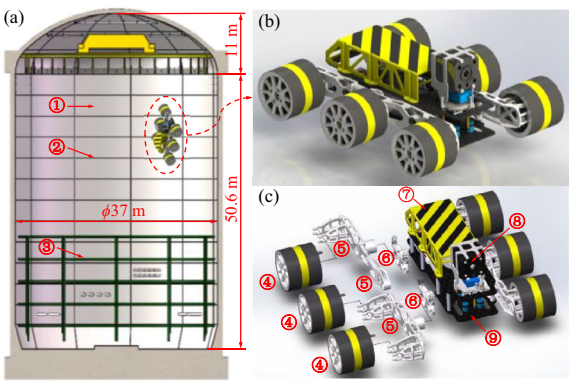

Figure 1 Structures of the nuclear power containment and NuBot. **a** Nuclear power containment, ① a plate of steel lining, ② weld, ③ support structure; **b** Axonometric view of the NuBot; **c** Exploded view of the NuBot, ④ magnetic adhesion wheel, ⑤ suspension, ⑥ support, ⑦ shell, ⑧ camera, ⑨ chassis

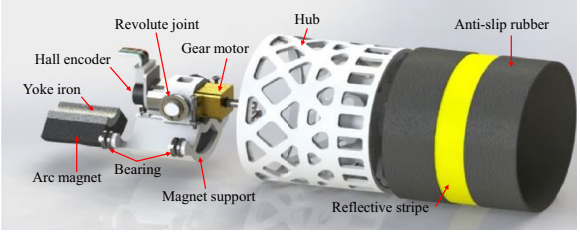

Figure 2 Exploded view of the magnetic adhesion wheel

axis. The magnet inside the wheel is installed under the motor, so the magnetic force will not change periodically as the wheel rotates.

A systematic design method is proposed to design and optimize the magnetic adhesion robot by comparison of various performance indices and specific application occasions: (1) Design the suspension type considering the adaptability, payload, and compliance. (2) Non-dimensional optimization of the suspension. Based on its kinematic model, proper indices such as workspace, payload, and stiffness are chosen to illustrate the performance in workspace, payload, and stiffness capacity. Eventually, optimum parameters with desired comprehensive performance in atlases are selected. (3) Non-dimensional optimization of the overall robot (including the wheel radius). Based on the dynamic model of the robot, the optimum parameters are selected through the adhesion stability on the steel lining. Thus, all non-dimensional parameters of the suspension and overall robot can be determined. (4) Obtaining actual dimension parameters considering the weld-seam traverse capability to determine the wheel radius, the smooth locomotion, and better curvature adaptability to derive the size of suspension and overall robot, and the interference-free conditions to constrain the bottom and top of the overall robot. (5) Magnet unit design in Maxwell, and overall structure and topological optimization are completed. (6) Experimental validation of the capabilities of surface-adaptability, adhesion stability, and payload of NuBot.

3 Type Design, Kinematics and Dynamics

3.1 Type Design of the Suspension

To ensure good motion and force properties, the design for the *wheeled locomotion suspension* of NuBot requires to meet multiple demands: (1) Good adaptability to the steel lining with varying geometrical morphology, including adapting to the curvature of the cylindrical wall, and also the uneven weld. The first-line importance is to keep all wheels in contact with the steel lining surface, so the robot can move more smoothly and steadily. (2) Good payload capability. The type design should enhance the load-weight ratio—carry more detection devices while possessing a lightweight structure. (3) Passive compliance

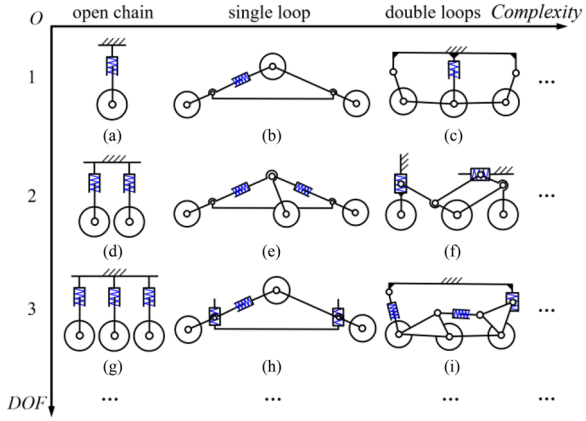

Figure 3 Type synthesis of the suspension mechanism based on the passive compliance utilizing cylindrical spring

rather than active compliance. It should utilize the energy component (cylindrical spring, coil spring, etc.) to passively match the deformation demands, and not utilize the motor in case of adding much weight and cost. Furthermore, NuBot takes the eudipleural structure on both sides, the base of suspension has a rigid connection with the robot body. So for the type synthesis of passive suspension based on the environmental adaptability of steel lining, the varying surface morphology is regarded as input that makes the length of spring-installed joint change, and the robot body is taken as output which has a significantly reduced fluctuation utilizing the designed suspension.

Based on the topological graph and the DOF equation, the number synthesis [31, 32] is implemented initially. Thereinto, Eq. (1) reveals the relations among the limb number k, the independent closed loop number L, the edge number e, the vertex number v; Eq. (2) reveals the relations among the DOF F_D, the motor number in the i th limb q_i $(i = 1 \sim n)$, the limb number k, the active limb number n, and the passive limb number p

$$L = e - v + k, \tag{1}$$

$$F_D = \sum_{i=1}^{n} (q_i - 1) + k - p. \tag{2}$$

To navigate on the irregular surface of steel lining, the six-wheeled NuBot is a feasible scheme with a good balance of adaptability and lightweight, considering the four-wheeled one reduces stability while the eight-wheeled one adds too much weight. Namely, each suspension should be installed with three wheels. So following the number synthesis, the type results of three-wheeled locomotion suspension are listed in Figure 3.

They have better adaptability to the irregular surface as the DOF increases along the vertical axis, and the types have more complexity with more loops and links along the horizontal axis.

Once many types of suspension have been obtained, the next work should be focused on the identification of the optimal one for practical application. The basic selection rules are as follows.

(1) The optimal type should satisfy the navigation demand on a complex surface: 3 DOF with motion characteristics of two translations and one rotation. Moreover, it is more preferred to employ the three-wheeled locomotion suspension based on the passive compliance utilizing cylindrical spring.
(2) The optimal type should adapt to the surface well and have a good mechanism stiffness. As shown in Figures 3(a, d, g), the wheel is connected to the robot body directly through a cylindrical spring. They just have an open-chain topology while not a closed-loop topology—a lower stiffness and adaptability.
(3) The optimal type should have fewer loops and fewer links. On one hand, the type with more loops and links has a strong motion non-linearity and complex force distribution; on the other hand, it produces more weight and doesn't make any particular significance for engineering practice.

Above all, Figure 3(h) is finally identified with a 3 DOF single-loop topology. Compared with the traditional independent suspension, it can guarantee real-time contact between the wheel and the steel lining, as well as a higher stiffness and adaptability.

3.2 Kinematic Modeling of the Suspension

After identifying the suspension type, the kinematic and dynamic models can be established. In Figure 4, $\{O\}$ denotes the suspension coordinate frame. In the mechanism view, l_4, l_5, l_6 are regarded as three inputs, and the relative motions (two translations and one rotation) of suspension with respect to the steel lining are regarded as outputs. Hence, B, C, and E are three independent point positions that can be chosen to install three locomotion wheels, as a reflection of three outputs.

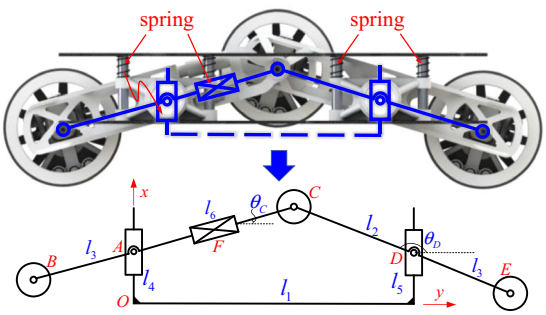

Figure 4 Sketch of the suspension structure and mechanism

Given B, C, and E are all taken as the outputs, so the position kinematics of the suspension can be defined by a loop-closure equation given as

$$\begin{cases} \boldsymbol{r}_{OA} + \boldsymbol{r}_{AC} = \boldsymbol{r}_{OD} + \boldsymbol{r}_{DC}, \\ \boldsymbol{r}_{OB} = \boldsymbol{r}_{OA} + \boldsymbol{r}_{AB}, \\ \boldsymbol{r}_{OE} = \boldsymbol{r}_{OD} + \boldsymbol{r}_{DE}, \end{cases} \tag{3}$$

where $\boldsymbol{r}_{OA}$ is a vector from O to A, and other vectors have the same naming rule.

Next, three differential kinematic equations can be derived to indicate the influence of outputs on the inputs. According to the theory of mechanism, the linkage between C and F has three DOFs, while AB and DE are 2-DOF linkages, due to the redundancy of the θ_C and θ_D. Inverse Jacobian matrix of C can be obtained as $\dot{\boldsymbol{q}} = \left[\dot{l}_4, \dot{l}_5, \dot{l}_6\right] = \boldsymbol{J}_{IK}^{C} \boldsymbol{v}_C$, where $\boldsymbol{q}$ denotes the input matrix, $\boldsymbol{J}_{IK}^{C}$ is the inverse Jacobian matrix obtained by Eq. (4), and $\boldsymbol{v}_C$ is the velocity of point C.

$$\begin{cases} \boldsymbol{J}_{IK}^{C} = \begin{bmatrix} -\tan\theta_C & 1 & -\frac{x_C}{\cos^2\theta_C} \\ \pm\frac{l_1 - x_C}{\sqrt{l_2^2 - (l_1 - x_C)^2}} & 1 & 0 \\ \frac{1}{\cos\theta_C} & 0 & \frac{x_C \sin\theta_C}{\cos^2\theta_C} \end{bmatrix}, \\ \boldsymbol{v}_C = \begin{bmatrix} \dot{x}_C \\ \dot{y}_C \\ \dot{\theta}_C \end{bmatrix}. \end{cases} \tag{4}$$

The inverse Jacobian matrices of linkages AB and DE can be obtained from pseudo-inverse of Jacobian matrices as $\boldsymbol{v}_B = [\dot{x}_B, \dot{y}_B]^{\mathrm{T}} = \boldsymbol{J}_{FK}^{B} \dot{\boldsymbol{q}}$, and $\boldsymbol{v}_E = [\dot{x}_E, \dot{y}_E]^{\mathrm{T}} = \boldsymbol{J}_{FK}^{E} \dot{\boldsymbol{q}}$, where $\boldsymbol{v}_B$ and $\boldsymbol{v}_E$ are the velocities of points B and E, and $\boldsymbol{J}_{FK}^{B}$ and $\boldsymbol{J}_{FK}^{E}$ are their Jacobian matrices obtained by Eqs. (5) and (6).

$$\boldsymbol{J}_{FK}^{B} = \begin{bmatrix} \kappa_1 \sin\theta_D & -\kappa_1 \sin\theta_D & \kappa_1 \cos(\theta_C - \theta_D) \\ 1 - \kappa_2 \sin\theta_D & \kappa_2 \sin\theta_D & -\kappa_2 \cos(\theta_C - \theta_D) \end{bmatrix}, \tag{5}$$

$$\boldsymbol{J}_{FK}^{E} = \begin{bmatrix} \kappa_4 \sin\theta_D & -\kappa_4 \sin\theta_D & \kappa_3 \sin\theta_D \\ \kappa_4 \cos\theta_D & 1 + \kappa_4 \cos\theta_D & -\kappa_3 \cos\theta_D \end{bmatrix}, \tag{6}$$

where

$$\kappa_1 = \frac{l_3 \sin\theta_C}{l_6 \sin(\theta_C - \theta_D)},$$
$$\kappa_2 = \frac{l_3 \cos\theta_C}{l_6 \sin(\theta_C - \theta_D)},$$
$$\kappa_3 = \frac{l_3}{l_2 \sin(\theta_C - \theta_D)},$$
$$\kappa_4 = \left(\cos\theta_D + \frac{\sin\theta_D}{\tan(\theta_C - \theta_D)}\right)\frac{l_3}{l_2}.$$

Hence

$$\boldsymbol{J}_{IK}^{B} = (\boldsymbol{J}_{FK}^{B})^{\dagger}, \boldsymbol{J}_{IK}^{E} = (\boldsymbol{J}_{FK}^{E})^{\dagger}, \tag{7}$$

where $\boldsymbol{J}_{IK}^{B}$ and $\boldsymbol{J}_{IK}^{E}$ represent the inverse Jacobian matrices of wheels B and E, and the symbol † denotes pseudo-inverse.

3.3 Dynamic Modeling of the Overall Robot

The dynamic model of the robot describes the relationship between the motor torques and the motion of NuBot, and can be further used to analyze the adhesion stability (Figure 5(a)) and the weld-crossing capacity on the inclined surface (Figure 5(b)).

Dynamics of the robot can be expressed by Lagrange formulation. The kinetic energy T_{OR} and the potential energy U_{OR} of the overall robot are obtained by

$$\begin{cases} T_{OR} = \frac{1}{2}\sum_{j=0}^{12} m_j {}^{G}\boldsymbol{v}_j^{T\,G}\boldsymbol{v}_j + \frac{1}{2}\sum_{j=0}^{12} {}^{G}\boldsymbol{\omega}_j^{T\,G}\boldsymbol{I}_j {}^{G}\boldsymbol{\omega}_j, \\ U_{OR} = -\sum_{j=0}^{12} m_j \boldsymbol{g}^{T\,G}\boldsymbol{p}_{cj} - \frac{1}{2}\sum_{j_k=1}^{6} k_s \Delta_{j_k}^2, \\ \quad {}^{G}\boldsymbol{p}_{cj} = {}^{G}\boldsymbol{p}_{c0} + {}^{G}\boldsymbol{R}_B {}^{B}\boldsymbol{p}_{cj}, \\ {}^{G}\boldsymbol{I}_j = \left({}^{G}\boldsymbol{R}_B {}^{B}\boldsymbol{R}_{P_j}\right) {}^{P_j}\boldsymbol{I}_j \left({}^{G}\boldsymbol{R}_B {}^{B}\boldsymbol{R}_{P_j}\right)^{\mathrm{T}}, \end{cases} \tag{8}$$

where $\{B\}$ is the coordinate frame located in the center of gravity (COG) of body, $\{G\}$ is the global coordinate frame. To arrange the sequence number of overall robot: $j = 0$ is the robot body, $j = 1 \sim 6$ are the wheels, $j = 7 \sim 12$ are the suspension parts, and $j_k = 1 \sim 6$ are the cylindrical springs. Furthermore, k_s and Δ_{j_k} are the rate and compression of the j_k th spring; $\boldsymbol{p}_{cj}$ is the COG position of the jth part; m_j, $\boldsymbol{v}_j$, $\boldsymbol{\omega}_j$ and $\boldsymbol{I}_j$ are the corresponding masses, linear velocities, angular velocities, moments of inertia; ${}^{G}\boldsymbol{R}_B$ is the orientation matrix of $\{B\}$ with respect to $\{G\}$, ${}^{B}\boldsymbol{R}_{P_j}$ is the orientation matrix of the jth link frame $\{P_j\}$ with respect to $\{B\}$, $\boldsymbol{g}$ is the gravitational acceleration.

Thus, the Lagrange function can be yielded by $L_{OR} = T_{OR} - U_{OR}$, indicating the composite effects of kinetic and potential energies, given by

$$\begin{cases} \frac{d}{dt}\left(\frac{\partial L_{OR}}{\partial \dot{q}_j}\right) - \frac{\partial L_{OR}}{\partial q_j} = R_w \tau_j - f_{\mathrm{fric}}^{j}, \\ \frac{d}{dt}\left(\frac{\partial L_{OR}}{\partial \dot{q}_{j_k}}\right) - \frac{\partial L_{OR}}{\partial q_{j_k}} = k_s \Delta_{j_k}, \end{cases} \tag{9}$$

where q_j and q_{j_k} are the generalized coordinates composed by the joint variables of wheels and springs respectively; R_w is the wheel radius; τ_j is the jth motor torque,

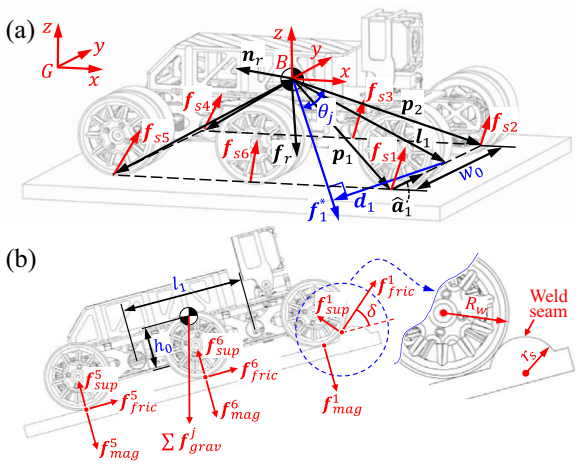

Figure 5 Dynamic force analysis: (**a**) Adhesion stability and (**b**) Weld-crossing ability of the robot

and f_{fric}^{j} is the friction between the jth wheel and steel lining surface.

4 Optimization Design Using PCbDM

To reveal the relations between the parameters (suspension mechanism and overall robot respectively) and performances of NuBot, the physical model and PCbDM method [25] are utilized for their visualization and global optimization merits. The physical model transforms the design variables from infinite solution space to finite solution space based on the non-dimensional operation, so that it lays the foundation for global optimization and finally requires solving the factor from the non-dimensional solution to the actual dimension parameters. And the PCbDM method provides an atlas-based formulation for the optimization process and result, and facilitates engineering optimization.

4.1 Non-Dimensional Optimization of the Suspension

To establish the optimization model of suspension, the design variables are l_1, l_2, l_3 for the sake that they are constants while l_4, l_5, l_5 are prismatic joint variables. Moreover, the constraint conditions are translational and rotational ranges of all joints. Last but not least, three criteria (i.e. objective functions) are employed to give a comprehensive performance evaluation on suspension:

(1) The workspace area index (WAI) is utilized to describe its motion range which determines the surface adaptability formed by three wheels to traverse the complex surface. The wheels should reach more areas to satisfy the needs of different situations, and can be expressed as

$$\eta_{\mathrm{W}} = \int_{\mathrm{S}} \mathrm{d}S = \int_{x_{\min}}^{x_{\max}} \mathrm{d}x \int_{y_{\min}}^{y_{\max}} \mathrm{d}y, \tag{10}$$

where $x \in [x_{\min}, x_{\max}]$ and $y \in [y_{\min}, y_{\max}]$ are the integral variables of the three outputs workspace.

(2) The global payload index (GPI) is used to evaluate the extremum payload force that the suspension can bear during locomotion. The suspension bears the most mass of the body and the force from the wheel centers. To obtain the suspension with a larger payload capacity, we use GPIs to evaluate the extremum force the suspension can bear during locomotion on uneven steel lining. The force equation is: $\boldsymbol{F} = \boldsymbol{G}\boldsymbol{\tau}$, where $\boldsymbol{F}$ is the output general force at wheel centers while $\boldsymbol{\tau}$ is the input general force at prismatic joint *A*, *D*, and *F*, and $\boldsymbol{G}_{IK}$ is the inverse force Jacobian matrix. From the relationship $\boldsymbol{G} = \boldsymbol{J}_{IK}^{-\mathrm{T}}$, the GPIs can be given by

$$\begin{cases} \eta_{F\max} = \dfrac{\int_S \sqrt{\max(|\lambda_{Fi}|)}\mathrm{d}S}{\int_S \mathrm{d}S}, \\ \eta_{F\min} = \dfrac{\int_S \sqrt{\min(|\lambda_{Fi}|)}\mathrm{d}S}{\int_S \mathrm{d}S}, \end{cases} \tag{11}$$

where λ_{Fi} are the eigenvalues of the matrix $\boldsymbol{G}^{\mathrm{T}}\boldsymbol{G}$.

(3) The global stiffness index (GSI) is used to evaluate the extreme linear displacement capacity. The suspension should possess larger mechanism stiffness to produce linear displacement in the input joints, so the robot can adapt to the terrain with the displacement of the input joints. Therefore, we use GSIs to evaluate the displacement deformation and hope them to be as larger as possible. The deformation equation is: $\boldsymbol{P} = \boldsymbol{C}\boldsymbol{F}$, where $\boldsymbol{P}$ is linear displacement deformation of the three prismatic joints, $\boldsymbol{C} = \boldsymbol{J}_{FK}\boldsymbol{J}_{FK}^{\mathrm{T}}$ are the compliance matrix. Therefore, the GSIs can be given by

$$\begin{cases} \eta_{P\max} = \dfrac{\int_S \sqrt{\max(|\lambda_{Pi}|)}\mathrm{d}S}{\int_S \mathrm{d}S}, \\ \eta_{P\min} = \dfrac{\int_S \sqrt{\min(|\lambda_{Pi}|)}\mathrm{d}S}{\int_S \mathrm{d}S}, \end{cases} \tag{12}$$

where λ_{Pi} are the eigenvalues of the matrix $\boldsymbol{C}^{\mathrm{T}}\boldsymbol{C}$.

There are three optimization parameters in the suspension model, including l_1, l_2 and l_3. The mean of the parameters is obtained by:

$$\frac{1}{3}(l_1 + l_2 + l_3) = T. \tag{13}$$

We can get the normalized equation by dividing both sides of equation by T:

$$t_1 + t_2 + t_3 = 3, \tag{14}$$

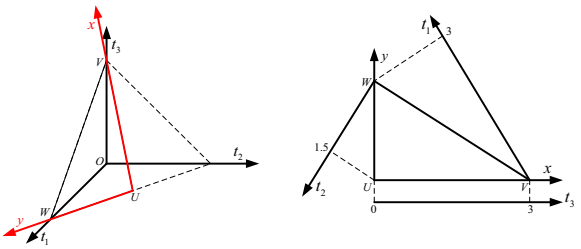

Figure 6 Parameter design space of the suspension

where $t_1 = \frac{l_1}{T}$, $t_2 = \frac{l_2}{T}$ and $t_3 = \frac{l_3}{T}$. Thus, the optimization parameters are converted to $t_i (i = 1, 2, 3)$.

Considering dimensional constraint $l_2 < l_1$, the constraint equations can be given as:

$$\begin{cases} t_2 < t_1, \\ 0 < t_1, t_3 < 3, \\ 0 < t_2 < 1.5. \end{cases} \tag{15}$$

Eqs. (14) and (15) show the parameter design space of the suspension, as shown in Figure 6.

The mapping function of variables between frame $O - t_1t_2t_3$ and frame $U - xyz$ can be given as

$$\begin{cases} x = \dfrac{3 - t_1 + t_2}{\sqrt{2}}, \\ y = \dfrac{3 - t_1 - t_2}{\sqrt{6}}. \end{cases} \tag{16}$$

Consequently, the ASI, GPI and GSI performance atlases of the suspension from wheel *B*, *C*, and *E* are shown in Figures 7, 8, 9 and 10, respectively.

The WAI performance atlases of three wheels are shown in Figure 7, where t_1, t_2, t_3 are the non-dimensional forms of l_1, l_2, l_3. One can see that wheel *B* has the smallest motion area, while wheel *C* has the largest area. Considering a larger output range to better adapt to the complex surface, the solution domain of WAI is assigned as $\Omega_{\mathrm{WAI}} = \{(t_1, t_2, t_3) | \eta_W^B \geq 0.2, \eta_W^C \geq 0.5, \text{and } \eta_W^E \geq 0.5\}$, where $\eta_W^B, \eta_W^C, \eta_W^E$ denote the WAI of wheels *B*, *C*, and *E*.

The GPIs (denoted as $\eta_{F\max}, \eta_{F\min}$) and GSIs (denoted as $\eta_{P\max}, \eta_{P\min}$) atlases of wheel *B* are shown in Figure 8. One can see that they show the different distribution principles with the design variables changing. Considering a larger payload capacity of suspension, the solution domain is assigned as $\Omega_{\mathrm{GPI}} = \{(t_1, t_2, t_3) | \eta_{F\min}^B \geq 0.2, \eta_{F\min}^C \geq 0.7, \eta_{F\min}^E \geq 0.5\}$. Likewise, due to better adaptability to the complex surface, the solution domain is assigned as $\Omega_{\mathrm{GSI}} = \{(t_1, t_2, t_3) | \eta_{P\min}^B \geq 0.5, \eta_{P\min}^C \geq 0.9, \eta_{P\min}^E \geq 0.3\}$.

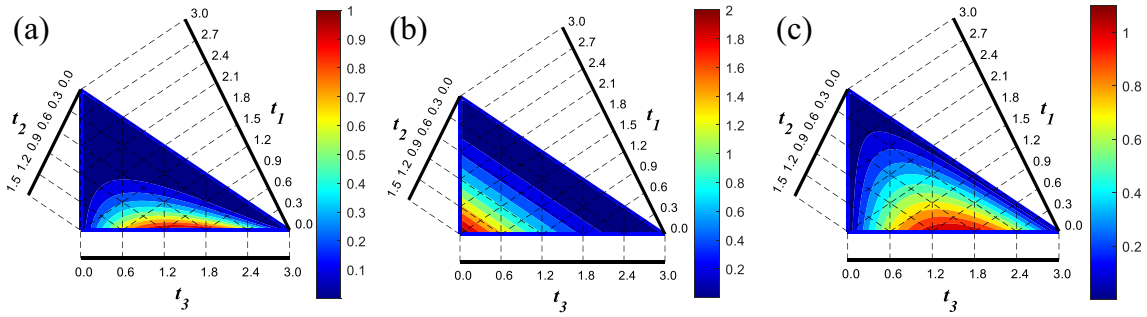

Figure 7 The suspension WAI performance atlases: (**a**) Wheel *B*, (**b**) Wheel *C*, (**c**) Wheel *E*

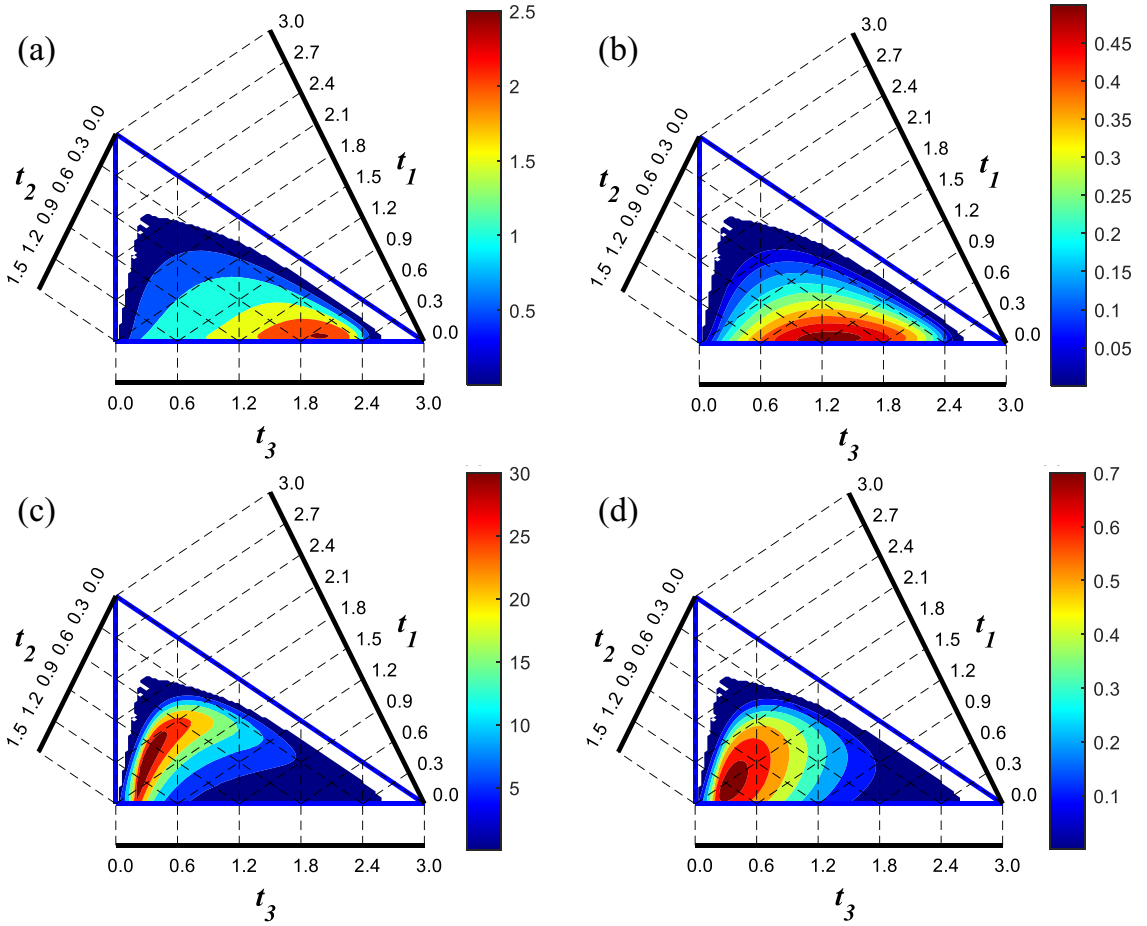

Figure 8 The suspension performance atlases of wheel *B*: (**a**) $\eta_{F\max}$, (**b**) $\eta_{F\min}$, (**c**) $\eta_{P\max}$, (**d**) $\eta_{P\min}$

The analysis method is also applicable to wheel *C* and wheel *E*. And the above results provide us with credible evidence to compare multiple parameters to satisfy the optimum comprehensive performances for the suspension. Hence, we can conclude that the optimum domain solution of the suspension (denoted as Ω_{susp}) is the intersection set of Ω_{WAI}, Ω_{GPI} and Ω_{GSI}. Further, if we assign each sub-domain (Ω_{WAI}, Ω_{GPI} or Ω_{GSI}) with more strict demands, then the size of Ω_{susp} will be smaller and smaller and tend to be a unique value. In this case, the global optimum non-dimensional solution is finally identified. Besides, it can also be assigned directly in Ω_{susp} according to the designer's initiative (Figure 11). Following a series of trade-offs among WAI, GPI, and GSI,

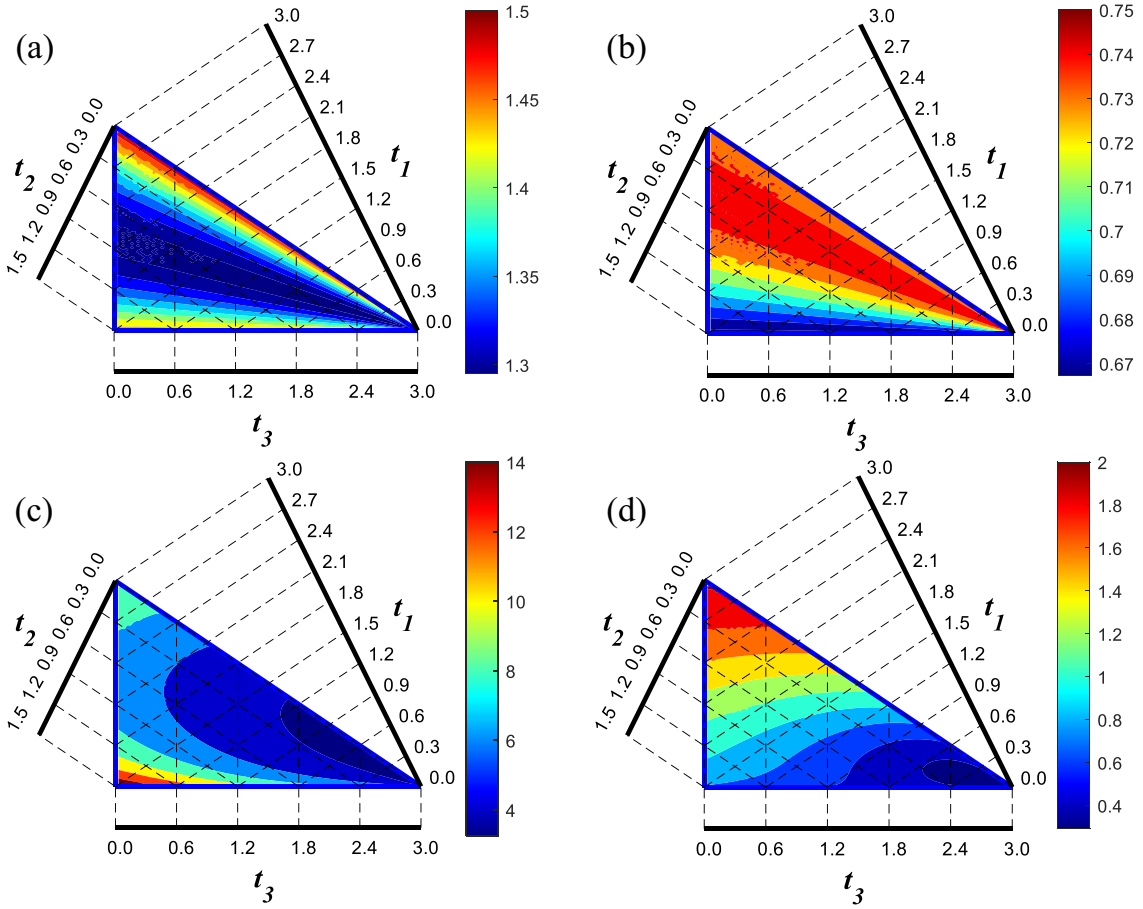

Figure 9 The suspension performance atlases of wheel *C*: (**a**) η_{Fmax}, (**b**) η_{Fmin}, (**c**) η_{Pmax}, (**d**) η_{Pmin}

the red star represents our final identification: the global optimum non-dimensional solution with $t_1 = 1.5$ and $t_2, t_3 = 0.75$, that is to say, $l_1 : l_2 : l_3 = 2 : 1 : 1$.

4.2 Non-Dimensional Optimization of the Overall Robot

The overall robot is comprised of two suspensions in parallel connection, so it is reasonable to be taken as a parallel mechanism; the body is the moving platform and the contact surface of steel lining is the static platform. To establish its optimization model, the design variables (Figure 5) include l_1, R_w, and the width of body w_0.

The adhesion stability is an important performance criterion, and affects the locomotion security of both robot and equipment inside the containment. It can be described as that the robot will not tip over across any line formed by two adjacent wheels. Based on the force-angle stability measure [33], the adhesion stability index (ASI) takes the resultant tipover force, support polygon, COG position, etc. into account simultaneously. Given the reliable magnetic adhesion to the steel lining surface, six wheels form a support polygon, and they together with the COG can eventually form a rectangular pyramid. Figure 5(a) illustrates the geometric analyses (support polygon $P_1P_2P_3P_4P_5P_6$, tipover axis $\widehat{\boldsymbol{a}}_j$ and its normal $\boldsymbol{l}_j$, tipover arm $\boldsymbol{d}_j$, tipover angle θ_j) and force analyses (wheel-surface resultant force $\boldsymbol{f}_{sj}$, tipover resultant force $\boldsymbol{f}_r$, tipover resultant moment $\boldsymbol{n}_r$, effective tipover resultant force $\boldsymbol{f}_j^*$) to evaluate the tipover cost of overall robot, which has an essential significance to move securely on the steel lining. According to the D'Alembert principle in Figure 5(a), the kineto-static equation is

$$\sum \boldsymbol{f}_{\text{grav}} + \sum \boldsymbol{f}^j_{\text{mag}} + \sum \boldsymbol{f}^j_{\text{sup}} + \sum \boldsymbol{f}^j_{\text{fric}} - \sum \boldsymbol{f}_{\text{iner}} = 0, \tag{17}$$

where $j = 1 \sim 6$ refers to the numbers of six wheels; $\boldsymbol{f}_{\text{grav}}$ is the gravitational load; $\boldsymbol{f}^j_{\text{mag}}$ is the magnetic adhesion force; $\boldsymbol{f}^j_{\text{sup}}$ is the support force applied to the contact points between wheel and surface, and $\boldsymbol{f}_{\text{iner}}$ is the inertial force. Notebly, $\boldsymbol{f}^j_{\text{mag}}$, $\boldsymbol{f}^j_{\text{sup}}$ and $\boldsymbol{f}^j_{\text{fric}}$ can only be applied to the six wheels, while $\boldsymbol{f}_{\text{grav}}$ and $\boldsymbol{f}_{\text{iner}}$ exist in all parts of the robot.

The general tipover resultant force $\boldsymbol{Q}_r$ acting on the COG may lead to a tipover instability, given by

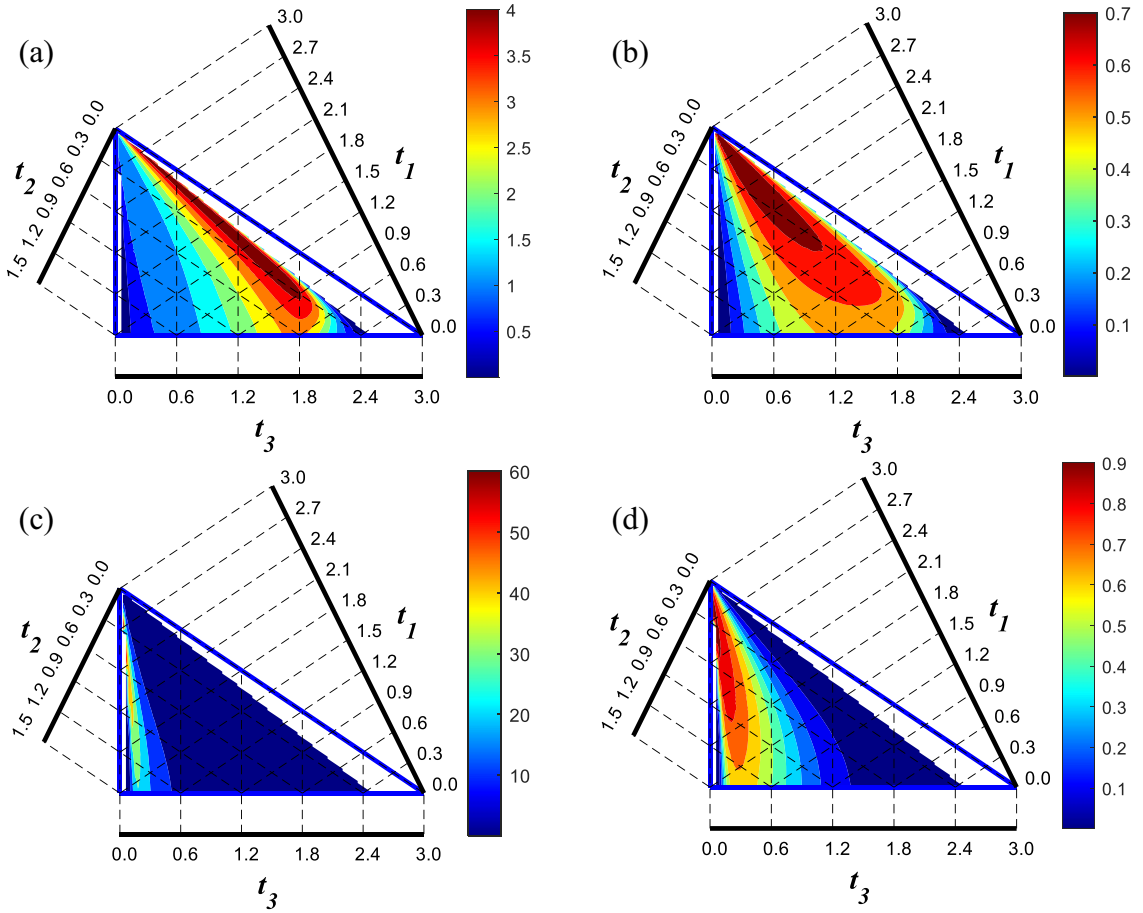

Figure 10 The suspension performance atlases of wheel *E*: (**a**) $\eta_{F\max}$, (**b**) $\eta_{F\min}$, (**c**) $\eta_{P\max}$, (**d**) $\eta_{P\min}$

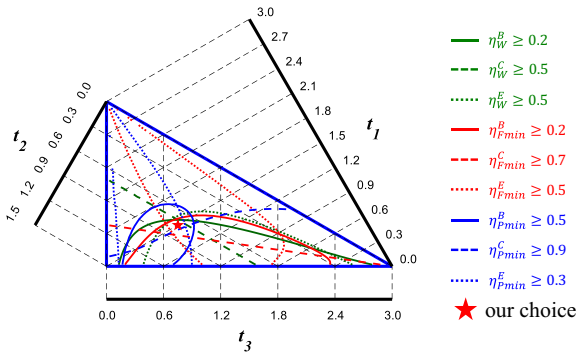

Figure 11 The global solution domain and the optimum solution of suspension

$$\boldsymbol{Q}_r = \begin{bmatrix} \boldsymbol{f}_r \\ \boldsymbol{n}_r \end{bmatrix} = \begin{bmatrix} \sum \boldsymbol{f}_{\text{grav}} + \sum \boldsymbol{f}_{\text{mag}}^j - \sum \boldsymbol{f}_{\text{iner}} \\ \boldsymbol{p}_j \times \left(\sum \boldsymbol{f}_{\text{grav}} + \sum \boldsymbol{f}_{\text{mag}}^j - \sum \boldsymbol{f}_{\text{iner}} \right) \end{bmatrix}, \tag{18}$$

where $\boldsymbol{p}_j (j = 1 \sim 6)$ is the position vectors of each vertex of the support polygon.

As the tipover resultant force $\boldsymbol{Q}_r$ has various unstable influences on various tipover axes $\widehat{\boldsymbol{a}}_j$. Hence, the relative tipover force component $\boldsymbol{Q}_{rj}$ with respect to the tipover axis $\widehat{\boldsymbol{a}}_j$ is extracted and given by

$$\boldsymbol{Q}_{rj} = \begin{bmatrix} \boldsymbol{f}_{rj} \\ \boldsymbol{n}_{rj} \end{bmatrix} = \begin{bmatrix} \left(\boldsymbol{I}_{3\times 3} - \widehat{\boldsymbol{a}}_j \widehat{\boldsymbol{a}}_j^T \right) \boldsymbol{f}_r \\ \left(\widehat{\boldsymbol{a}}_j \widehat{\boldsymbol{a}}_j^T \right) \boldsymbol{n}_r \end{bmatrix}, \tag{19}$$

where $\widehat{\boldsymbol{a}}_j$ is the j th unit tipover axis vector from $\boldsymbol{p}_j$ to $\boldsymbol{p}_{j+1}$ and $\widehat{\boldsymbol{a}}_j = \left(\boldsymbol{p}_{j+1} - \boldsymbol{p}_j \right) / \| \boldsymbol{p}_{j+1} - \boldsymbol{p}_j \|$.

Next, $\boldsymbol{n}_{rj}$ is transformed into an equivalent force couple $\left(\widehat{\boldsymbol{l}}_j \times \boldsymbol{n}_{rj} \right) / \| \boldsymbol{l}_j \|$ ($\boldsymbol{l}_j$ is the tipover axis normal with respect to $\widehat{\boldsymbol{a}}_j$ and $\boldsymbol{l}_j = \left(\boldsymbol{I} - \widehat{\boldsymbol{a}}_j \widehat{\boldsymbol{a}}_j^{\mathrm{T}} \right) \boldsymbol{p}_{j+1}$) lying in the normal plane of $\boldsymbol{n}_{rj}$, so as to formulate a unified expression considering both effects of $\boldsymbol{f}_{rj}$ and $\boldsymbol{n}_{rj}$. Therefore, the

effective tipover resultant force $\boldsymbol{f}_j^*$ with respect to the tipover axis $\widehat{\boldsymbol{a}}_j$ is given by

$$\boldsymbol{f}_j^* = \boldsymbol{f}_{rj} + \frac{1}{\|\boldsymbol{l}_j\|}\left(\widehat{\boldsymbol{l}}_j \times \boldsymbol{n}_{rj}\right). \tag{20}$$

Herein, the ASI (η_s) is defined to evaluate the average adhesion stability of the robot in a posture with all configurations of the suspension by

$$\eta_s = \frac{\int \mu_s \mathrm{d}W}{\int \mathrm{d}W}, \mu_s = \min_j\left(\theta_j \cdot \|\boldsymbol{d}_j\| \cdot \|\boldsymbol{f}_j^*\|\right), \tag{21}$$

where μ_s denotes the FASM; $\mathrm{d}W$ is the traversal of the suspension workspace; θ_j is the tipover angle, and the negative value indicates the robot will tip over along the jth axis directly; $\boldsymbol{d}_j$ denotes the tipover radius vector; $\boldsymbol{f}_j^*$ is the resultant tipover force.

The means of the optimization parameters l_1, w_0, and R_w are obtained by

$$\frac{1}{3}(l_1 + w_0 + R_w) = U. \tag{22}$$

We can get the normalized equation by dividing both sides of the equation by U

$$u_1 + u_2 + u_3 = 3, \tag{23}$$

where $u_1 = \frac{l_1}{U}$, $u_2 = \frac{w_0}{U}$, and $u_3 = \frac{R_w}{U}$. Thus, the optimization parameters are converted to u_1, u_2, u_3.

Considering dimensional constraint $R_w < w_0 < 2l_1$, the constraint equations can be given as

$$\begin{cases} u_3 < u_2 < 2u_1, \\ 0 < u_3 < 1.2. \end{cases} \tag{24}$$

Eqs. (13) and (14) show the parameter design space of the suspension, as shown in Figure 12.

During the locomotion process, the NuBot experiences various postures affected by the complex surface of the steel lining. Thereinto, the complete handstand posture is the most dangerous one. Herein, the mass of the

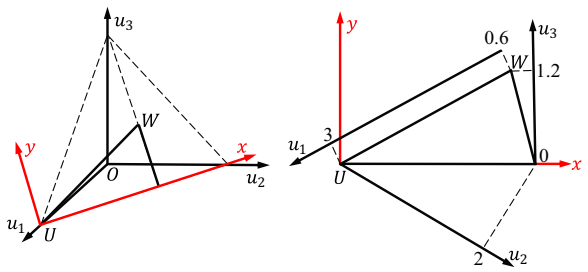

Figure 12 Parameter design space of the overall robot

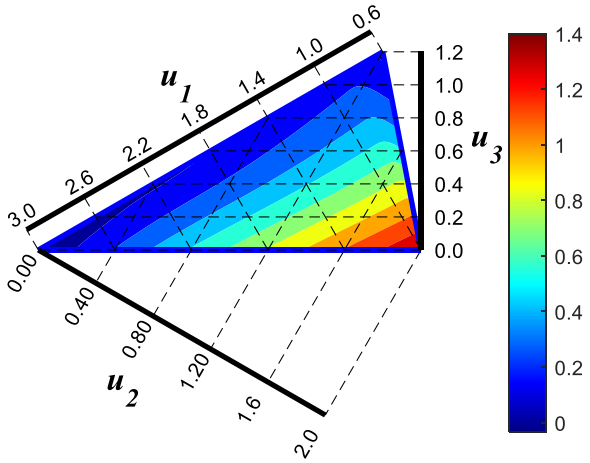

Figure 13 The ASI performance atlases of the overall robot

suspension and the inertial force of the robot are ignored for simplification, and the magnetic force increases gradually until the negative value disappears in the ASI performance. Figure 13 shows the ASI performance atlas, where u_1, u_2, u_3 are the non-dimensional parameters corresponding to l_1, w_0, R_w.

The ASI atlas shows that there are three ways to improve the adhesion stability of overall robot, i.e., larger length of suspension, larger width of support polygon, and smaller radius of the wheel. We can conclude that $u_1 = 1$, $u_2 = 2$ and $u_3 = 0$ is the optimal choice, that is, $w_0 = 2l_1$ and $R_w = 0$. Although in practice, R_w is limited by the actual size and cannot be zero, this suggests that the height of COG should be minimized as much as possible.

4.3 Identification of Actual Dimensions by Working Condition

The above obtain the optimum proportion relations among all design variables of both suspension and overall robot, i.e. $l_1 : l_2 : l_3 : w_0 = 2 : 1 : 1 : 4$. In the following, we will first solve the normalization factor to transform the non-dimensional solution to actual dimension parameters; according to the working conditions inside the environment of steel lining, we will finally obtain these actual dimension parameters. Three major aspects should be taken into account.

(1) The weld-seam traverse capability requires to meet the contact angle condition. Eq. (25) illustrates that a small wheel radius R_w or weld radius r_s, or a big weld height h_s can make a large contact angle δ between wheel and weld, further resulting to make all wheels slippery and unable to traverse the weld seam. Eq. (26) illustrates that the friction force of

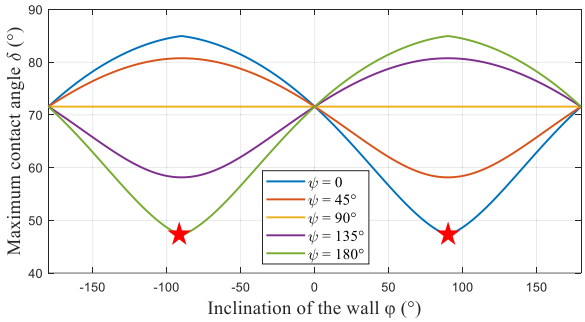

Figure 14 Relations among the maximum contact angle, wall inclination angle, and yaw angle

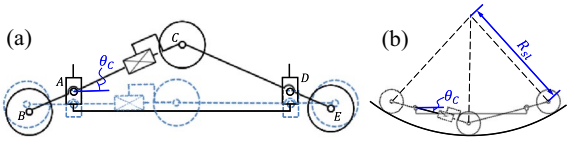

Figure 15 Configurations of the suspension: (**a**) The middle wheel crosses the weld, (**b**) The robot moves on curved surface

wheel-surface contact has a maximum limit to avoid slip.

$$\delta = \arccos\left(\frac{R_w + r_s - h_s}{R_w + r_s}\right) \le \delta_m, \tag{25}$$

$$f_{fric}^j \le \mu_s f_{sup}^j, \tag{26}$$

where μ_s is the sliding friction coefficient, $\mu_s = 0.5$.

Moreover, considering the critical slipping condition, a force equilibrium equation can be derived by Eq. (17) regardless of the inertial force term. Thus, the maximum contact angle for a successful traverse under various wall inclination angle is obtained in Figure 14. One can see the minimum δ_m is 47.2° when φ is around ±90°, so the actual contact angle must be no more than δ_m.

Summing up the above extreme conditions for traversing successfully, the maximum arc weld seam has a height $h_s = 5$ mm and radius $r_s = 11.8$ mm, and the allowable δ_m is assigned to be 31°. As a result, we can derive $R_w = 27$ mm according to Eq. (25).

(2) The orientation fluctuation quantity caused by the weld-seam height (Figure 15(a)), and the minimum steel lining radius of curvature R_{sl} that NuBot can adapt to (Figure 15(b)) should be reduced as little as possible. To ensure smooth locomotion and better curvature adaptability, $|\theta_C|$ and R_{sl} is chosen to evaluate the orientation fluctuation and minimum steel lining radius, and smaller values are desired.

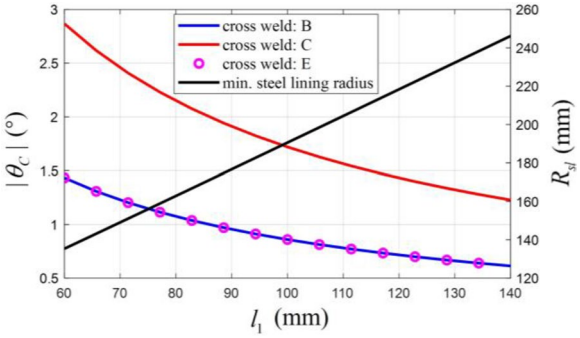

Figure 16 The orientation fluctuation and minimum radius of curvature when the robot crosses the weld and adapts to steel lining

The relationship between $|\theta_C|, R_{sl}$ and l_1 can be derived by geometry relationship. The interference-free conditions of adjacent wheels can be expressed by

$$\begin{cases} 2R_w \le l_3 + l_6, \\ 2R_w \le l_2 + l_3, \\ 2R_w \le (l_3 + l_6)\cos\theta_C - (l_2 + l_3)\cos\theta_D. \end{cases} \tag{27}$$

Considering each configuration of the suspension, eventually $l_1 \ge 54$ mm is obtained. After leaving some gap, the travel range of l_1 is finally chosen to be 60–140 mm. The results of the above cases are shown in Figure 16.

One can see that: when crossing the weld, $|\theta_C|$ decreases as l_1 increases, while R_{sl} shows the opposite change when the robot adapts to the curved steel lining. After making a trade-off between the two cases, l_1 is chosen to be 100 mm.

Hence, the other two lengths of the suspension are given by $l_2 = l_3 = 50$ mm, and parameters of the robot are given by $w_0 = 2l_1 = 200$ mm.

(3) The interference-free conditions considering the weld seam and support structure effects constrain the bottom and top of the overall robot. To avoid interference between the chassis and weld seam, the initial height of the bottom chassis h_{bc} and the travel ranges of l_4 and l_5 should be as large as possible (Figure 15(a)), which in turn causes higher COG and smaller ASI. Thus, the limit case is considered and h_{bc}, l_4 and l_5 are respectively chosen to be 15 mm, 10 mm, and 10 mm after trade-off.

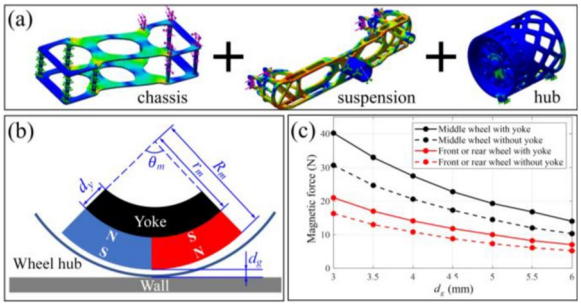

Figure 17 **a** Topological optimization results of the chassis, suspension, and wheel hub, **b** Structure of the magnet unit, **c** The relationship between magnetic force and wall distance

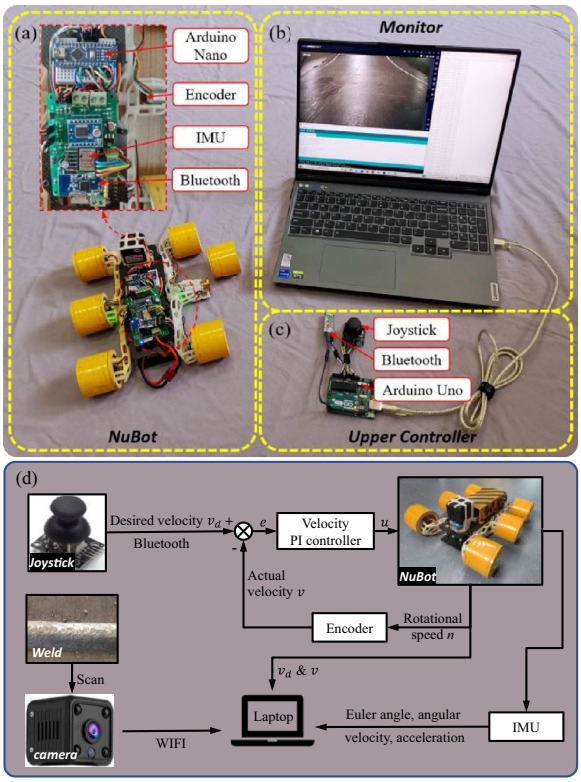

Figure 18 Schematic of electronic components and the control strategies. **a** Microcontroller and sensors inside NuBot, **b** The monitor for displaying weld images and sensor data, **c** The upper controller for controlling locomotion of NuBot, **d** The closed-loop

5 Unit Design and Prototype

With all sizes determined, the rest parameters regarding mass, magnet, etc. can be determined through the following steps: (1) obtaining the robot mass after designing and topological optimization of the structure; (2) designing the magnet unit in Maxwell software.

(1) The overall robot can be designed with corresponding parameters proportion. To reduce weight, all structural components including chassis, suspension, and the wheel hub are obtained by topological optimization and finite element simulation in the software of solidThinking Inspire (Figure 17(a)). Considering the weight of the electronic components, the overall mass of NuBot is around 1 kg.

(2) Next, the parameters of magnet can be determined by simulation in Maxwell (Figure 17(b)), including the radius of magnet R_m, r_m, the angle of sector magnet θ_m, the thickness of yoke d_y, and the gap distance between the magnet and the wall. Considering the magnetic force is supposed to support the entire robot and ensure certain safety, the design magnetic force is set to be 55 N. Simulation shows that the magnet weight is 75% less than the magnet with a full circle, but the magnetic force only decreases by 15%. To reduce steering friction [6], per middle wheel shares twice the magnetic force of a front or rear wheel. Figure 17(c) shows that the magnetic force decreases when the gap distance increases, and the 6 mm gap that satisfies the desired force is finally selected. The detailed sizes of the magnet unit are shown in Table 2.

So far, all design parameters and specific structures of NuBot can be determined, and the prototype composed of six magnetic wheels, two pairs of suspensions, and a platform is developed, as shown in Figure 18. And the specifications of NuBot are listed in Table 3.

The control system is shown in Figure 18(d). The Arduino Uno works as an upper machine, which

Table 2 Specifications of the sector magnets

Wheel	R_m (mm)	r_m (mm)	Axial thickness (mm)	θ_m (°)	d_y (mm)	Simulated magnetic force (N)
Front/rear	17.6	9.9	20	90	3	6.96
Middle			30			13.75

Table 3 Specifications of NuBot platform

Items	Features
Total mass	980 g
Partial mass	Front/rear wheel: 72 g Middle wheel: 80 g Suspension: 32 g Others: 468 g
Length × width × height	$260 \times 200 \times 100\,\text{mm}^3$
Length of wheelbase	100 mm
Radius of wheel	27 mm
Joint limits of suspension	$l_4, l_5 \in [0, 10\text{mm}]$ $\theta_C \in [-15°, 15°]$
Material	Carbon fiber board (chassis) 3D printing resin (other body parts)
DC motor (encoder inside)	Type: GA12-N20 (0.2 Nm) Max. angular speed: 120 r/min
Controller	Arduino Uno (upper machine) Arduino Nano (lower machine)
IMU	JY901 (9-axis: accelerometer, gyroscope, and magnetometer)

transmits desired speed to the lower machine through Bluetooth. The Arduino Nano works as a lower machine, which processes data from encoders and IMU, and controls driving motors through a speed PI controller. Speeds of the wheels are read from the encoders and the closed-loop control is formed by comparison with the desired speed from the joystick. All the components are powered by an 11.1 V and 3000 mAh battery, and can work continuously for more than 30 min. The camera works independently with the above control system, which will not be described in detail for it is secondary here. Sensor data and weld images can be transmitted to the laptop for monitoring.

6 Experimental Results and Discussion

6.1 Locomotion on Different Types of Walls

Figures 19(a, b) show the locomotion on a strong magnetic curved wall with a radius of 2 m. The maximum speed of NuBot is 0.5 m/s, which is around 1.92 times the robot length. Due to the strong magnetic force, the robot can only turn with a radius of 3 m. Please see the Additional file 1: Video. Figure 19(c) shows the locomotion on the weak magnetic blackboard, and the minimum turning radius is 0.2 m. The magnetic force herein is around one-third of that on the curved wall. Locomotion experiments on the blackboard with various inclination angles are conducted in Figures 19(d–f), which validate the adhesion stability of NuBot.

Experiments on the vertical blackboard are conducted to test the precise movement. Given desired

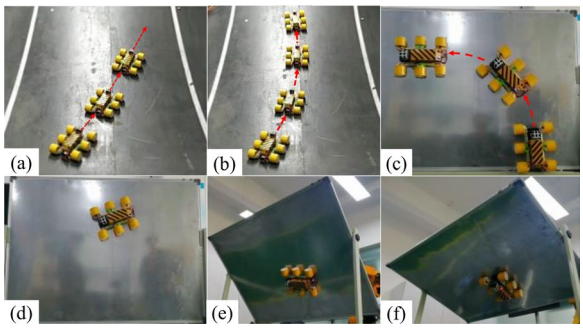

Figure 19 Locomotion experiments. **a** Moving forward, **b** Steering on a strong magnetic curved wall; **c** Steering on a weak magnetic blackboard; locomotion on the blackboard with an inclination angle of (**d**) 90°, (**e**) 135°, and (**f**) 180°

wheel speed on both sides, the desired trace can be obtained. The actual trace is calculated by accumulating the mileage from encoders inside the left and right wheels. As shown in Figure 20, the robot turns around a circle at a constant speed. The actual trace coincides well with the expected one, and the trace radius error tends to be a minor value.

6.2 Validation of Weld-crossing Capacity

Crossing the welds on the containment surface may cause instability of the robot body, which in turn affects the adhesion stability. Herein we tested this process with 3D printed welds with two typical heights of 3 mm and 5 mm (the maximum weld height), as shown in Figure 21. Results show that the crossing process hardly affects the adhesion stability of the robot.

Another function of the suspension is to reduce the fluctuation of the robot body when crossing uneven terrain. Herein, when the robot crosses the weld, the change of its body pitch angle is recorded by IMU, as shown in Figure 22. In general, the theoretical and experimental results fit well before the peak, while after the peak, the suspension makes the body stabilize quickly. And the maximum peak error is within 9%.

6.3 Validation of Payload Capacity

Payload capacity is a significant index of the climbing robot. Herein, experiments on payload capacity under different walls are conducted, as shown in Figure 23. The maximum load of the robot on the blackboard is 0.6 kg with a speed of 0.08 m/s (Figure 23(a)), and the wheels will slip when the load continues to increase. Besides, the load on the curved wall reaches 0.8 kg with a speed of 0.065 m/s (Figure 23(b)). In either case, the robot can load enough weight of the equipment for weld inspection.

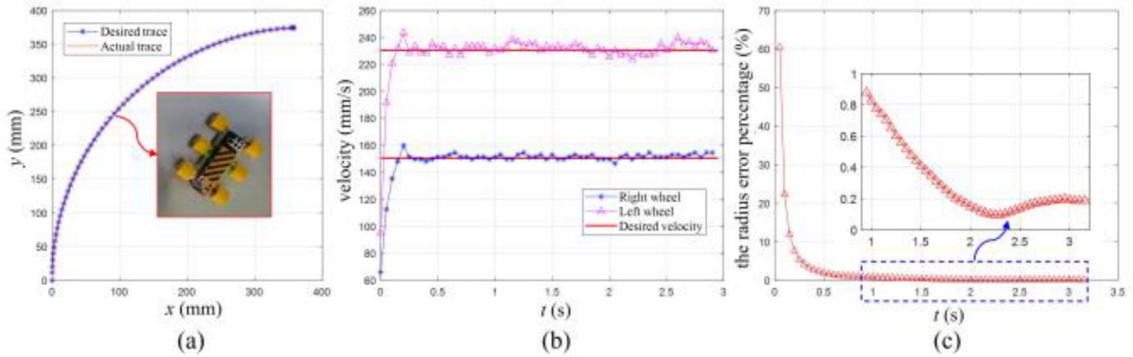

Figure 20 Steering motion accuracy experiments. **a** Comparison between the actual trace and desired trace (desired radius is 375 mm), **b** Change of left and right wheel speed (desired wheel speed: left 230 mm/s and right 150 mm/s), **c** Error percentage of trace radius

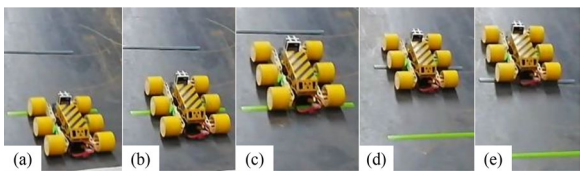

Figure 21 Weld crossing experiments. The robot crosses the weld with a height of (**a**–**c**): 3 mm; (**d**–**e**): 5 mm

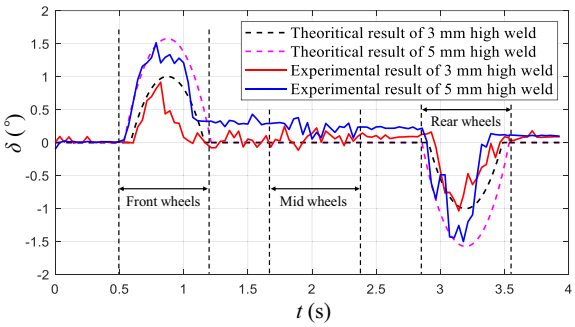

Figure 22 Comparison of theoretical and experimental results of the body pitch when crossing the weld

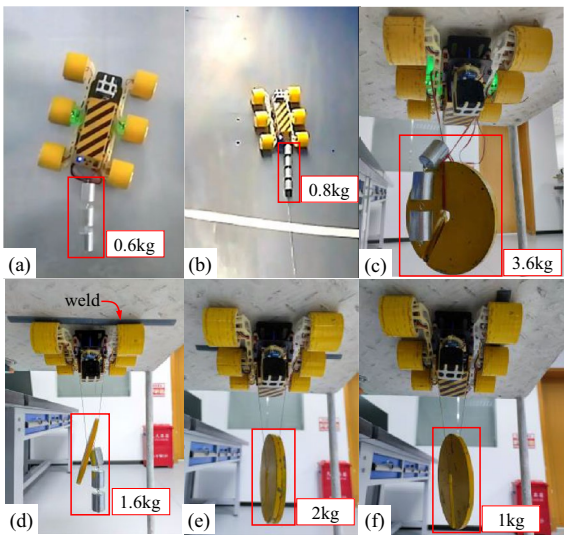

Figure 23 Payload capacity experiments: **a** Locomotion on the vertical blackboard, **b** Locomotion on curved wall, **c** Static adhesion to the inverted wall, **d**–**f** Crossing the weld on inverted wall by two front, middle, lateral wheels

Besides, extreme payload experiments are conducted to verify the payload capacity (Figures 23(c–f), namely cases 1 to 4). The case of robot handstand is selected, because the influence of wheel friction can be ignored, and we can focus on the influence of adhesion stability on the robot. Figure 24 illustrates the magnetic force, corresponding ASI, and experimental maximum load under the four cases. As expected, NuBot in case 1 possesses the maximum payload of up to 3.6 kg. Notably, the magnetic force in case 4 is not the smallest, but the payload capacity is the worst, which indicates the asymmetry of magnetic force distribution will reduce the payload capacity.

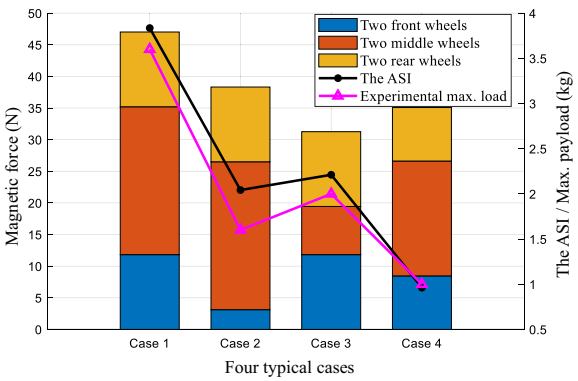

Figure 24 The magnetic force under different cases in experiment

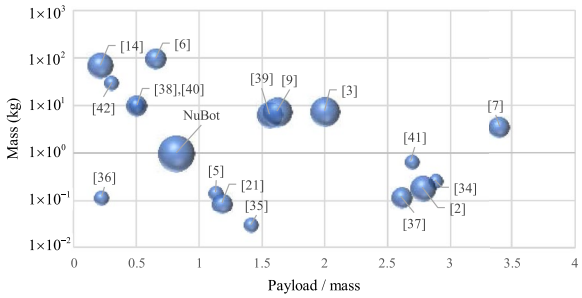

Figure 25 Comparison of payload/mass, mass, and number of driving motors of several typical climbing robots, where the bubble size represents the number of driving motors

6.4 Results and Discussion

The experimental results show that NuBot can carry a 0.6 kg load on the weak magnetic wall and a load of no less than 0.8 kg on the strong magnetic wall with a radius of 2 m. The actual trace has a small error compared to the desired one. Besides, the robot reaches a maximum load of 3.6 kg, which is 3.67 times its mass, and the experimental results of its maximum payload are consistent with the analysis of ASI. In addition, the robot can stably cross the simulated welds and move on the walls with different inclination angles.

The payload capacity is an important indicator of its performance and can be evaluated by the ratio of the payload to its mass. Robots that can carry more load with less of their mass are favored. Figure 25 shows a comparison of the performances of several climbing robots. Notably, the weight of robots with soft bodies or footpads [2, 5, 21, 34–37] are all less than 1 kg, moreover, robots in [2, 34, 37] are with an excellent payload capacity of more than 2.5 times their weight. By contrast, wheeled [6, 7, 9, 38] or crawler [3, 14, 39, 40] magnetic adhesion robots are heavier due to the mechanical components. Particularly, NuBot obtained under our design strategy has a light body with a good payload capacity, and the number of driving motors ensures it has sufficient driving force.

7 Conclusions

This paper proposes a magnetic adhesion robot with passive suspension and six wheels called NuBot, which is used to inspect the steel lining weld of the ferromagnetic wall (nuclear power containment is chosen as an application here). The main contribution of this article is to establish a systematic design method for the wheeled adhesion robot.

(1) A 3-DOF suspension with good adaptability to the steel lining, good payload capability, and passive compliance is proposed, which ensures that the robot adapts to the curvature of the steel lining.
(2) Building a comprehensive optimization design model for NuBot. Based on the kinematic model of suspension and the dynamic model of the overall robot, the optimization model is established, including the parameters of topological structure and the performance indices of WAI, GPI, GSI, and ASI. Then, the PCbDM is applied to optimize NuBot with five parameters from the suspension (local) to the overall robot (whole). Optimal parameters are properly chosen from the performance atlases perceptually and credibly.
(3) The normalization factor and actual dimension parameters are determined by constraints of the working conditions inside the environment of the steel lining.

The electronic system with a PI controller is constructed to accomplish a higher control accuracy. Critical experiments are conducted to validate the design and recorded as a video, seen in the Additional file 1. The experimental results show that NuBot meets the comprehensive requirements on size, weight, locomotion, payload, and adhesion stability.

Applications of NuBot can be further expanded. On the one hand, the robot can be equipped with more inspection instruments, such as ultrasonic flaw detectors, magnetic flaw detectors, etc. And devices that exceed the robot payload can be equipped by the hard connection of several robots. On the other hand, NuBot can be used on more occasions with ferromagnetic walls, such as oil and gas tanks and pipelines, vessels, and wind turbines. NuBot can be modified to adapt to the specific environment constraints based on the proposed design method.

Supplementary Information

The online version contains supplementary material available at https://doi.org/10.1186/s10033-023-00905-6.

Additional file 1. Experimental video.

Acknowledgements

The authors sincerely thanks to Professor Shaohong Zhang of Shanghai Nuclear Star Nuclear Power Technology Co., Ltd. for his critical discussion during design of the robot and prototype.

Author Contributions

HX conducted the detailed study on the theoretical analysis of the robot, and completed the experiment and manuscript writing; YH put forward the idea of theoretical analysis and participated in the writing of manuscript; MH modeled the robot structure and made the prototype. YL participated in the experiment and paper writing; WG gave overall guidance during analysis, design, and experiments of the robot, and writing of the manuscript. All authors read and approved the final manuscript.

Authors' Information
Hao Xu, born in 1997, received his master degree from *State Key Lab of Mechanical System and Vibration, School of Mechanical Engineering, Shanghai Jiao Tong University, China*, in 2023.
Youcheng Han, born in 1993, is currently a PhD candidate at *State Key Lab of Mechanical System and Vibration, School of Mechanical Engineering, Shanghai Jiao Tong University, China*.
Mingda He, born in 1998, is currently a Mechanical Engineer in *Shenzhen Dajiang Innovation Technology Co., Ltd., China*. He received his master degree from *State Key Lab of Mechanical System and Vibration, School of Mechanical Engineering, Shanghai Jiao Tong University, China*, in 2022.
Yinghui Li, born in 1999, is currently a PhD candidate at *State Key Lab of Mechanical System and Vibration, School of Mechanical Engineering, Shanghai Jiao Tong University, China*.
Weizhong Guo, born in 1970, is currently a professor and a PhD candidate supervisor at *State Key Lab of Mechanical System and Vibration, School of Mechanical Engineering, Shanghai Jiao Tong University, China*. His main research interests include modern mechanism, parallel robot, motion planning and design.

Funding
Supported by Shanghai Nuclear Star Nuclear Power Technology Co., Ltd., National Natural Science Foundation of China (Grant No. 51735009), and State Key Lab of Mechanical System and Vibration Project (Grant No. MSVZD202008).

Availability of Data and Materials
The datasets supporting the conclusions of this article are included within the article.

Declarations

Ethics Approval and Consent to Participate
Not applicable.

Consent for Publication
Not applicable.

Competing Interests
The authors declare no competing financial interests.

Received: 29 May 2022 Revised: 5 June 2023 Accepted: 8 June 2023
Published online: 17 August 2023

References

[1] H Sun. *Third generation nuclear power technology AP1000*. Beijing: China Electric Power Press, 2010.
[2] T Seo, M Sitti. Tank-like module-based climbing robot using passive compliant joints. *IEEE/ASME Transactions on Mechatronics,* 2013, 18(1): 397-408.
[3] F Gao, J C Fan, L Zhang, et al. Magnetic crawler climbing detection robot basing on metal magnetic memory testing technology. *Robotics and Autonomous Systems*, 2020, 125: 103439.
[4] Y Guan, H Zhu, W Wu, et al. A modular biped wall-climbing robot with high mobility and manipulating function. *IEEE/ASME Transactions on Mechatronics,* 2013, 18: 1787-1798.
[5] Y Liu, H Kim, T Seo. Anyclimb: a new wall-climbing robotic platform for various curvatures. *IEEE/ASME Transactions on Mechatronics,* 2016, 21: 1812-1821.
[6] W Song, H Jiang, T Wang, et al. Design of permanent magnetic wheel-type adhesion-locomotion system for water-jetting wall-climbing robot. *Advances in Mechanical Engineering,* 2018, 10(7): 168781401878737.
[7] F Tâche, W Fischer, G Caprari, et al. Magnebike: a magnetic wheeled robot with high mobility for inspecting complex-shaped structures. *Journal of Field Robotics,* 2009, 26(5): 453-476.
[8] M Tavakoli, L Marques, A T de Almeida. OmniClimber: an omnidirectional light weight climbing robot with flexibility to adapt to non-flat surfaces. *IEEE/RSJ International Conference on Intelligent Robots & Systems*, 2012, 61(9): 280-285.
[9] H Eto, H H Asada. Development of a wheeled wall-climbing robot with a shape-adaptive magnetic adhesion mechanism. *IEEE International Conference on Robotics and Automation (ICRA)*, Paris, France, September, 2020: 9329-9335.
[10] J Guo, K Lee, D Zhu et al. Large-deformation analysis and experimental validation of a flexure-based mobile sensor node. *IEEE/ASME Transactions on Mechatronics,* 2012, 17(4): 606-616.
[11] J Fan, T Xu, Q Fang, et al. A novel style design of a permanent-magnetic adsorption mechanism for a wall-climbing robot. *Journal of Mechanisms and Robotics,* 2020, 12(3): 1-30.
[12] G Lee, G Wu, J Kim, et al. High-payload climbing and transitioning by compliant locomotion with magnetic adhesion. *Robotics and Autonomous Systems,* 2012, 60(10): 1308-1316.
[13] G Liu, Y Liu, X Wang, et al. Design and experiment of a bioinspired wall-climbing robot using spiny grippers. *IEEE International Conference on Mechatronics and Automation,* Harbin, China, September 2016: 665-670.
[14] G Lee, H Kim, K Seo, et al. MultiTrack: a multi-linked track robot with suction adhesion for climbing and transition. *Robotics and Autonomous Systems,* 2015, 72: 207-216.
[15] A T Asbeck, S Kim, M R Cutkosky, et al. Scaling hard vertical surfaces with compliant microspine arrays. *The International Journal of Robotics Research,* 2006, 25(12): 1165-1179.
[16] P Birkmeyer, A G Gillies, R S Fearing. Dynamic climbing of near-vertical smooth surfaces. *IEEE/RSJ International Conference on Intelligent Robots & Systems*, Vilamoura-Algarve, Portugal, December, 2012: 286-292.
[17] K Carpenter, N Wiltsie, A Parness. Rotary microspine rough surface mobility. *IEEE/ASME Transactions on Mechatronics,* 2016, 21(5): 2378-2390.
[18] H Wang, A Yamamoto, T Higuchi. A crawler climbing robot integrating electroadhesion and electrostatic actuation. *International Journal of Advanced Robotic Systems,* 2014, 11(12), 1-11.
[19] G Gu, J Zou, R Zhao, et al. Soft wall-climbing robots. *Science Robotics,* 2018, 3(25): 2874.
[20] S Kim, M Spenko, S Trujillo, et al. Whole body adhesion: hierarchical, directional and distributed control of adhesive forces for a climbing robot. *IEEE International Conference on Robotics & Automation*, Rome, Italy, May, 2007: 1268-1273.
[21] M P Murphy, C Kute, Y Mengüç, et al. Waalbot II: adhesion recovery and improved performance of a climbing robot using fibrillar adhesives. *The International Journal of Robotics Research,* 2011, 30(1): 118-133.
[22] M Zhang, X Zhang, M Li, et al. Optimization design and flexible detection method of a surface adaptation wall-climbing robot with multisensor integration for petrochemical tanks. *Sensors,* 2020, 20(22): 6651.
[23] Y Liu, M Shin, K Jeong, et al. Dry adhesion optimization design for a wall-climbing robot based on experiment. *International Conference on Ubiquitous Robots and Ambient Intelligence (URAI)*, Kuala Lumpur, Malaysia, March, 2014: 216-219.
[24] J Hoff, A Ramezani, S Chung, et al. Optimizing the structure and movement of a robotic bat with biological kinematic synergies. *The International Journal of Robotics Research,* 2018, 37(10): 1233-1252.
[25] X Liu and J Wang. A new methodology for optimal kinematic design of parallel mechanisms. *Mechanism and Machine Theory,* 2007, 42(9): 1210-1224.
[26] F Xie, X Liu, J Wang. A 3-DOF parallel manufacturing module and its kinematic optimization. *Robotics and Computer-Integrated Manufacturing*, 2012, 28(3): 334-343.
[27] F Xie, X J Liu, Z You, et al. Type synthesis of 2T1R-type parallel kinematic mechanisms and the application in manufacturing. *Robotics and Computer-Integrated Manufacturing*, 2014, 30(1): 1-10.
[28] Q Li, Z Chen, Q Chen, et al. Parasitic motion comparison of 3-PRS parallel mechanism with different limb arrangements. *Robotics and Computer-Integrated Manufacturing*, 2011, 27(2): 389-396.
[29] N Zhang, P Huang, Q Li. Modeling, design and experiment of a remote-center-of-motion parallel manipulator for needle insertion. *Robotics and Computer-Integrated Manufacturing*, 2018, 50: 193-202.
[30] Y Han, W Guo, Z Peng, et al. Dimensional synthesis of the reconfigurable legged mobile lander with multi-mode and complex mechanism topology. *Mechanism and Machine Theory*, 2021, 155: 104097.

[31] Z. Deng, H. Gao and L. Ding. *Design of mobility systems for lunar rovers*. Beijing: Higher Education Press, 2015.
[32] X Meng, F Gao, Q J Ge. Number synthesis of parallel robotic mechanisms. *Mechanics Based Design of Structures and Machines*, 2014, 42(2): 211-228.
[33] E Papadopoulos, D A Rey. The force-angle measure of tipover stability margin for mobile manipulators. *Vehicle System Dynamics*, 2000, 33(1): 29-48.
[34] Y Liu, B Lim, J W Lee, et al. Steerable dry-adhesive linkage-type wall-climbing robot. *Mechanism and Machine Theory*, 2020, 153: 103987.
[35] H Wang, A Yamamoto. Analyses and solutions for the buckling of thin and flexible electrostatic inchworm climbing robots. *IEEE Transactions on Robotics*, 2017, 33(4): 889-900.
[36] O Unver, M Sitti. Flat dry elastomer adhesives as attachment materials for climbing robots. *IEEE Transactions on Robotics*, 2009, 26(1): 131-141.
[37] O Unver, M Sitti. Tankbot: A palm-size, tank-like climbing robot using soft elastomer adhesive treads. *The International Journal of Robotics Research*, 2010, 29(14): 1761-1777.
[38] J Shang, B Bridge, T Sattar, et al. Development of a climbing robot for inspection of long weld lines. *Industrial Robot: An International Journal*, 2008, 35: 217-223.
[39] G Lee, G Wu, S H Kim, et al. Combot: Compliant climbing robotic platform with transitioning capability and payload capacity. *IEEE International Conference on Robotics and Automation*, Saint Paul, America, May, 2012: 2737-2742.
[40] H Huang, D Li, Z Xue, et al. Design and performance analysis of a tracked wall-climbing robot for ship inspection in shipbuilding. *Ocean Engineering*, 2017, 131: 224-230.